ACS APPLIED MATERIALS & INTERFACES

Research Article

www.acsami.org

A Simple Way To Achieve Pattern-Dependent Tunable Adhesion in Superhydrophobic Surfaces by a Femtosecond Laser

Dongshi Zhang, Feng Chen,* Qing Yang, Jiale Yong, Hao Bian, Yan Ou, Jinhai Si, Xiangwei Meng, and Xun Hou

State Key Laboratory for Manufacturing System Engineering and Key Laboratory of Photonics Technology for Information of Shaanxi Province, School of Electronics and Information Engineering, Xi'an Jiaotong University, Xi'an, 710049, People's Republic of China

Supporting Information

ABSTRACT: In this paper, we present a new approach to the tunable adhesive superhydrophobic surfaces consisting of periodic hydrophobic patterns and superhydrophobic structures by femtosecond (fs) laser irradiation on silicon. The surfaces are composed of periodic hydrophobic patterns (triangle, circle, and rhombus) and superhydrophobic structures (dual-scale spikes induced by a fs laser). Our results reveal that the adhesive forces of as-prepared surfaces can be tuned by varying the area ratio ($AR_{s\text{-}h}$) of superhydrophobic domain to hydrophobic domain, thus resulting in tunable static and dynamic wettabilities. By increasing $AR_{s\text{-}h}$, (i) the static wetting property, which is characterized by the minimum water droplet volume that enables a droplet to land on the surface, can be tailored from 1 μL to 9 μL; (ii) the sliding angle can be flexibly adjusted, ranging from >90° (a droplet cannot slide off when the sample is positioned upside down) to 5°; and (iii) the droplet rebound behaviors can be modulated from partial rebound to triple rebound. In addition, the Cassie–Baxter model and the sliding angle model are used to speculate the contact angles and sliding angles to provide potentially theoretical models to design slippery-to-sticky superhydrophobic surfaces. The tunable adhesive superhydrophobic surfaces achieved by fs laser microfabrication may be potentially used in microfluidic systems to modulate the mobility of liquid droplets.

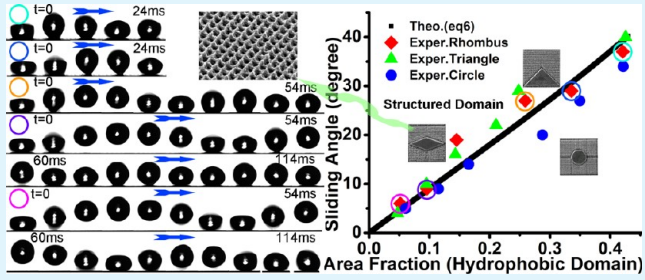

KEYWORDS: *femtosecond laser, superhydrophobic surface, tunable wettability, silicon spikes, superhydrophobic–hydrophobic pattern, water drop rebound*

1. INTRODUCTION

Nature has illustrated a wide variety of superhydrophobic surfaces with low or high adhesive forces. Low-adhesive superhydrophobic surfaces are characterized by water contact angle (CA) larger than 150° and sliding angle (SA) less than 10°.[1] Water droplets on such surfaces can easily roll off to remove loosely adherent dirt particles and debris from the surfaces if the substrate is slightly tilted. This phenomenon is well-known as the self-cleaning effect or lotus effect for its original discovery on natural lotus leaf.[2] Other than low-adhesive superhydrophobic surfaces, sticky or high-adhesive superhydrophobic surfaces characterized by both large SA and CA, represent another appealing branch of study.[3] A typical example of sticky natural species is rose petal,[4] which exhibits remarkable adhesive force with water droplet sticking to the surface even when it is positioned upside down.

Recently, intense interest has been focused on the smart superhydrophobic surfaces exhibiting tunable adhesive forces and SAs.[5] Zhu et al. realized slippery-to-sticky superhydrophobic surfaces by tuning the topographies of polyimide (PI) nanotube arrays using the porous alumina membrane molding method.[6] Li et al. have prepared CuO superhydrophobic surfaces ranging from extremely low to very high tunable adhesive force by a combination of solution-immersion process and fluoroalkylsilane coating.[7] Liu et al. reported the photoregulated stick–slip switch of water droplet mobility by using a photoresponsive coating on anodized alumina blank substrate.[8] Su et al. reported a facile route to reversibly tune surface wettability of $In_xGa_{1-x}N$ (InGaN) nanotip arrays by octylphosphonic acid (OPA) modification and ultraviolet–visible (UV–vis) light illuminations.[9] Nanoscale water interaction with tungsten nanorods generated under various Ar pressures and substrate tilting angles by using a glancing-angle deposition technique have also shown tunable hydrophobic properties after their surfaces were modified with a thin layer of Teflon.[10] By adjusting the deposition time, dissolution time, concentration ratio, and solution concentration, Li et al. also prepared a series of copper nanowire arrays with tunable wetting behaviors via redox reaction through infiltrating aqueous solutions of metal chloride salts into native porous anodic aluminum oxide template.[11] Teisala found that variation in the hierarchical structure of TiO_2 nanoparticle surfaces

Received: July 5, 2012
Accepted: August 21, 2012
Published: August 21, 2012

generated by the liquid flame spray (LFS) on board and paper substrates could contribute to varying droplet adhesion between the high- and low-adhesive superhydrophobic states.[12] In addition, tunable-SA superhydrophobic surfaces may realize the control of drop mobility and can be used for lab-on-paper (LOP) applications, such as drop storage, transfer, mixing, and sampling.[13] The reason why intelligent surfaces with tunable wetting properties attract increasing attention is that such surfaces can be applied to many fields, including nonloss liquid transportation,[14] cell adhesion,[15] and microfluidic channels with diminished resistance. Despite these successful fabrications of slippery-to-sticky surfaces, the structures are almost in nanoscale and the corresponding fabrication technologies suffer from the shortcomings of high cost, complexity, and necessity of masks. It is still expected to explore a facile production technology to fabricate tunable surfaces with simultaneously dual micro/nanoroughness similar to natural species.[16]

Femtosecond (fs) laser micromachining has proved to be a promising method to fabricate superhydrophobic surfaces for its unique ability to simultaneously fabricate hierarchical micro/nanoscale structures.[17] For example, Zorba et al. induced periodic lotus-leaf-like conical spikes by fs laser irradiation in gaseous SF_6 and found that the droplets' rebound behaviors on the spike surface were similar to that of lotus leaf.[18] Femtosecond laser can also be applied to a variety of materials to achieve hydrophobic, superhydrophobic, and even superhydrophilic surfaces, such as polymer,[19] metals,[20] and semiconductors.[21] Furthermore, the combination of fs laser microfabrication and digital control three-dimensional (3D) stages enables the preparation of various complicate patterns to manipulate a droplet's morphology. Our previous work revealed that, through adjusting the interval of periodic triangular array and strips, anisotropy wetting could be tuned.[22,23] The triangular silicon islands fabricated by the fs laser can realize mutual wetting transitions between anisotropic and isotropic.[24] In addition, fs laser treatment can also enhance the wettability of the surface without additional deposition of chemical layer to reduce the surface energy. For example, Kietzig et al.[25] found out that the alloys with initially smooth, hydrophilic surfaces could become nearly superhydrophobic or even superhydrophobic over time after fs laser irradiation. Bandoki et al. found the CA of alloys (Ti-6Al-V) would increase 50° after surface modification by the fs laser.[26] However, little is known about the realization of intelligent surface with tunable wettability via fs laser irradiation.

In this paper, we present a facile method to realize intelligent surfaces with tunable adhesion that can well modulate the CAs, SAs, and water droplet rebound behaviors. These surfaces are composed of superhydrophobic structures (spikes induced by the fs laser) and hydrophobic array (triangle, rhombus, and circle). Different area ratio (AR_{s-h}) of superhydrophobic domain to hydrophobic domain is investigated to show its influence on the surfaces' wettabilities. The energy barriers of these surfaces are analyzed, based on which both triple-phase contact lines (TPCLs) of water droplets and the dynamic TPCL evolution process are depicted. In addition, the Cassie–Baxter model and the sliding angle model are used to predict CAs and SAs.

2. EXPERIMENTAL SECTION

Surface Laser Irradiation. A Ti:sapphire laser-system (FEMTOPOWER compact Pro) with a pulse width of 30 fs at a fundamental wavelength 800 nm, a repetition rate of 1 kHz was used. The pulse energy on the sample was adjusted by a neutral density (ND) attenuator .The laser beam was subsequently focused with a microscope objective lens (20×, NA = 0.45, Nikon) into the sample (dimensions = 5 mm × 5 mm × 0.5 mm), which was mounted on a precision computer-controlled *x*-*y*-*z* translation stage with step resolution of 50 nm and a maximum speed of 3 mm/s. The schematic of the experimental setup is shown in ref 23.

Structured Patterns. Figure 1 shows a schematic illustration of the configurations used to fabricate triangular, circular, and rhombic

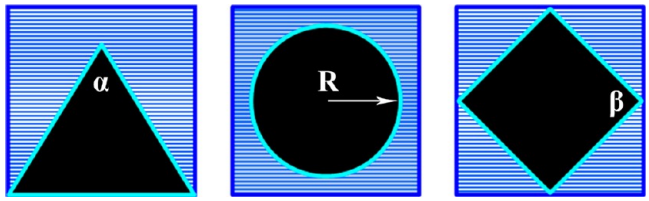

Figure 1. Schematic illustration of the fabrication of hierarchical structure.

patterns on *p*-doped (100) silicon wafers. Each pattern is fixed in a square matrix (as dark blue line denotes) with a matrix length constant of 500 μm. The line-by-line scanning method is employed to fabricate these patterns.[22] The light blue line denotes the scanning route. After laser irradiation, the unstructured domain turns out to be a triangular, circular, or rhombic pattern, as black domains denote in Figure 1. The laser energy is 13 mW and the scanning speed is 1 mm/s, in which case the laser spot size is 12 μm. The interval of adjacent laser scanning lines is 2 μm. By adjusting the triangle vertex α, circle radius R, and rhombus angle β, the area ratio of unstructured domain to structured domain can be modulated. The wettabilities of the structured/unstructured domains change from both hydrophilic (18°/45°) to superhydrophobic/hydrophobic (>150°/110°) after fluoroalkylsilane coating. The formula used to calculate the hydrophobic area fraction (η) in each matrix, with respect to each pattern, is, respectively,

Triangle:

$$\eta = \frac{ctg(\alpha/2)}{4}$$

Circle:

$$\eta = \frac{\pi R^2}{L^2}$$

Rhombus:

$$\eta = \frac{ctg(\beta/2)}{2}$$

The Sample Treatment. We used *p*-doped Si wafers. After structuring the silicon substrates in an air atmosphere by fs laser irradiation, the samples were cleaned by ultrasonic cleaning in water at 40 °C for 15 min, and then by a 15-min ultrasonic bath in acetone and in methanol in sequence. Immediately afterward, the samples were immersed into fluoroalkylsilane solution with a concentration of 2% for 2 h and then were roasted in a furnace with a temperature constant of 300 °C for another 12 h.

Morphology Analysis and Contact Angle Characterization. The morphology of the surface structures is analyzed using scanning electron microscopy (SEM) and optical microscopy (Model LV100D, Nikon). Contact angle characterization is performed using a Dataphysics Model OCA20 contact angle goniometer with an automated drop dispenser, and image and video capture system. The digital drop image is processed by the image analysis system, which calculates both the left and right contact angles from the drop shape with an accuracy of ±0.1°. Static water contact angle images are captured by the video. The large volume water droplet is measured

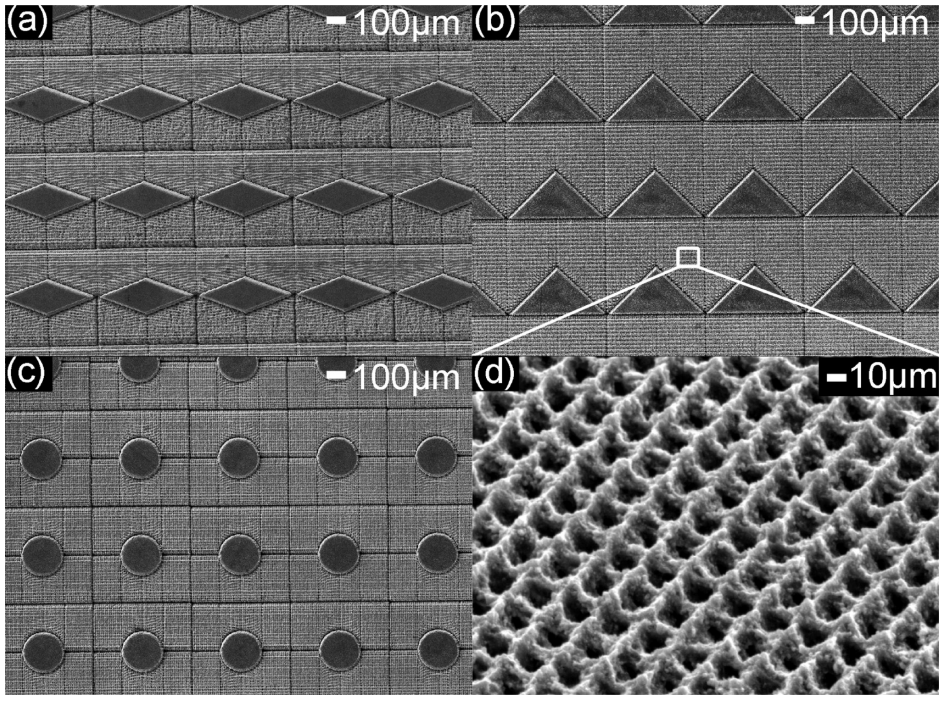

Figure 2. (a–c) SEM images of rhombic, triangular, and circular patterns fabricated by a femtosecond laser on Si. (d) Large magnification SEM image of the structures irradiated by a femtosecond laser.

usign a tangent algorithm instead of a spherical cap algorithm for the deformation of droplet due to the gravity of the droplet, which has been analyzed in detail in our previous paper.[23]

3. RESULTS AND DISCUSSION

Morphology of Structured Surface. Figure 2a–c shows SEM images of the laser-structured silicon surface consisting of periodic rhombic, triangular, and circular arrays. Each pattern is located in a 500-μm-wide square grid. The fs laser-structured domain is characterized by self-organized periodic conical spike forests with tens or hundreds of nanometer-sized protrusions. The period of the spikes is 10 μm. The spikes are considered to evolve from the microscale ridges.[27,28] The as-prepared surfaces were coated with a layer of of fluoroalkylsilane. The structured and unstructured domains then became superhydrophobic and hydrophobic, respectively. To describe the surfaces with different pattern array precisely, the surface with pure spikes is defined as the s-surface, and the surfaces with triangular, circular, and rhombic pattern arrays are defined as the t-surface, c-surface, and r-surface, respectively.

Static Contact Angles. To show how the wetting properties vary after the introduction of different hydrophobic patterns, the static and dynamic wettabilities of the s-surface are illustrated in Figure 3. When a 1-μL water droplet contacts the lifted s-surface, the suspending droplet is found to be very difficult to fall on the surface, even when the droplet is deformed severely by the upward pushing force during s-surface elevation. As the s-surface is moved downward, the droplet will depart from the sample and be taken away by the microsyringe. With the increase of water dose from 1 μL to 9 μL with step of 1 μL, the water droplet is still unable to land on the surface. When the water volume reaches 10 μL, the droplet detaches from the microsyringe, falls on the sample under the gravitation effect, and instantaneously rolls off (see Movie S1 in the Supporting Information). The conventional sessile droplet method is invalid to calculate static CAs when the droplet is

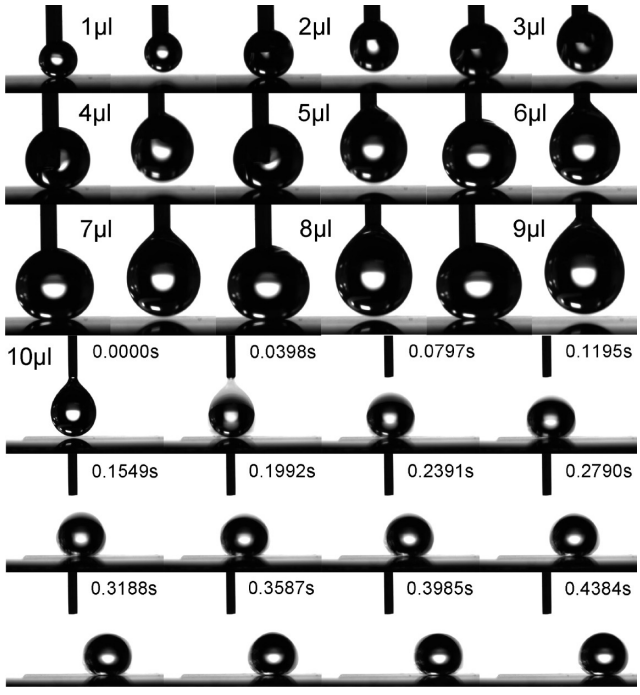

Figure 3. Response of 1–10 μL water droplets on the s-surface.

unable to land on the surface. In this case, Jiang et al. defined CA as 180°.[29] In addition, the SA of the s-surface is calculated to be 1°.

The excellent superhydrophobicity of the s-surface is considered to arise from the multiporous structures (Figure 2d). When a water droplet is placed on the s-surface, the droplet will only contact the protuberance of the spikes. Meanwhile, many air bubbles are trapped in the cavities, thus greatly reducing the contact area between the water droplet and the sample. The air bubbles function as an air cushion to hold

up the water droplet and make the s-surface become superhydrophobic.

Table 1 shows the minimum water volume (V_L) that allows a droplet to land on the t-/c-/r-surface at η values of 0.5, 0.25, 0.1918, 0.1443, 0.1036, 0.0672, and 0.0329. The specific calculation formula of η for each pattern is illustrated in the Experimental Section.

Table 1. Minimum Water Volume (V_L) That Enables a Droplet to Sit on the t-/c-/r-Surface at Different η Values and the Corresponding Static Contact Angles (CAs)

	Triangle		Circle		Rhombus	
η	CA (deg)	V_L (μL)	CA (°)	V_L (μL)	CA (°)	V_L (μL)
0.5	134	1	136	1	138	1
0.25	146	2	149	2	144	2
0.1918	150	3	150	3	149	3
0.1443	151	4	151	4	152	4
0.1036	155	5	152	5	153	5
0.0672	158	7	155	7	157	7
0.0329	160	9	160	9	161	9

With respect to the t-surface, at η = 0.5, the first 1-μL water droplet is able to sit on the surface and the static CA is 134°. As η decreases, more water volume is needed to enable the water droplet to land on the t-surface, with 1 μL (η = 0.5) increasing to 9 μL (η = 0.0329) (see Movie S2 in the Supporting Information). In the meantime, further decreases in η also lead to the static CA increasing from 134° to ~160°.

Figure 4 shows the water drop behaviors at η = 0.0329 on the t-surface. The 1−8-μL water droplets are unable to land on the surface, just like the case of the s-surface. However, note that the drop behavior on the t-surface is different from that on the s-surface when the droplet detaches from the sample. At V_L = 4−8 μL, the droplet shakes intensely hanging on the microsyringe just after its detachment from the t-surface, while a droplet detaches from the s-surface smoothly (see Figure 3). The water drop behaviors on the c-/r-surface exhibit wetting performances that are very similar to that of t-surface, as demonstrated in Table 1. These results demonstrate that the hydrophobic domains actually contribute to the water adhesion force while superhydrophobic domains contribute to the water repellent force. And the adjustment of the ratio of hydrophobic domain to superhydrophobic domain can tune the adhesive force of the surfaces.

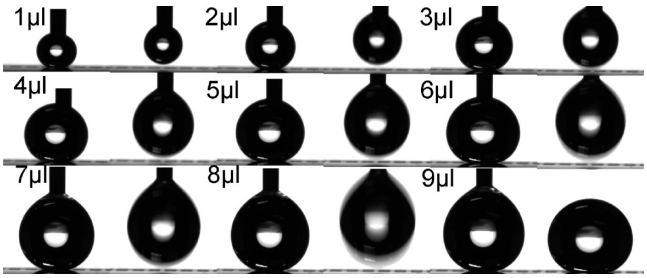

Figure 4. Graphic showing that 1−9-μL water droplets tend to land on the t-surface at η = 0.0329.

Free Energy Barrier Analysis. The surface roughness plays a crucial role in the superhydrophobic performance. The surface heterogeneity often gives rise to free-energy barriers (FEBs),[30−32] which will cause triple-phase contact line (TPCL) pinning or depinning behaviors of a water droplet.[33,34] When a droplet advances or recedes, it must overcome the FEBs where the droplet settles.[35,36] To better understand the wetting behaviors of the t-/c-/r-surface, the clarification of FEBs is essential.

Water evaporation on structured patterns has been proven to be an effective method to clarify the surface's FEBs.[22] Here, the FEBs are also explored by monitoring the dynamic evaporation behaviors of a droplet that is positioned on the as-prepared surfaces. The captured images are shown in Figure 5, where the droplet's morphologies are marked by a red line. It can be seen that the droplet retreats from the fourth triangle's edge to the third in the longitudinal direction (see Figures 5a and 5b, and Movie S3 in the Supporting Information), indicating that two corners along the triangular baseline play the FEBs role. Figure 5c and 5d indicates that a water droplet recedes from the fourth column of the triangular array to the third, resulting in the wetting transition from anisotropic to isotropic (see Movie S4 in the Supporting Information). This dynamic behavior indicates that the baseline, vertex angle, and bevel edge play the FEBs role. In addition, a series of jump-stick behaviors on the t-surface will realize the mutual wetting transitions between isotropic and anisotropic.[24] Because of the similarity between the triangle and rhombus shapes, it can be deduced that the four corners of the rhombus function as the FEBs.

As demonstrated in Figure 5, when a water droplet is placed on a hydrophobic substrate with periodic superhydrophobic domains, the droplet tends to wet the hydrophobic domains but dewet the superhydrophobic domains. The wetting phenomenon is very similar to the jump-stick behaviors on the surface with periodic hydrophobic pattern, on which a droplet sits on hydrophobic pillars and air pockets.[36] It can be deduced that the superhydrophobic domains on the t-/c-/r-surface actually play the same role of air. Correspondingly, the t-/c-/r-surface can be assumed to be a surface consisting of periodic hydrophobic pillars in different shape (triangle, circle, and rhombus) with the gap filling up with air. The wetting properties on circular pillars have been previously studied by Wong and Ho,[37] who point out the outward arc of the circles where the droplet settles plays the FEBs role.

Area Ratio Calculation. Wetting properties can be explained theoretically by two models. One is the Wenzel model,[38] which assumes that a liquid drop totally penetrates the structured surface and the liquid−solid CA θ_w follows the equation

$$\cos\theta_w = r\cos\theta \quad (1)$$

where r is the surface ratio between the overall surface area and the projected structured surface, θ is the intrinsic CA of the flat substrate. The other model is the Cassie−Baxter model,[39] which assumes that a water droplet only wets a small fraction of a rough surface with air pockets trapped under it and the static CA θ_{CB} can be predicted by

$$\theta_{CB} = \varphi_s(\cos\theta + 1) - 1 \quad (2)$$

φ_s denotes the area ratio. With respect to composite surfaces consisting of two different materials with different wettabilities, just like our t-/c-/r-surfaces, the CA θ_{CB} value is given by

$$\theta_{CB} = f_1\cos\theta_1 + f_2\cos\theta_2 \quad (3)$$

$$f_1 + f_2 = 1$$

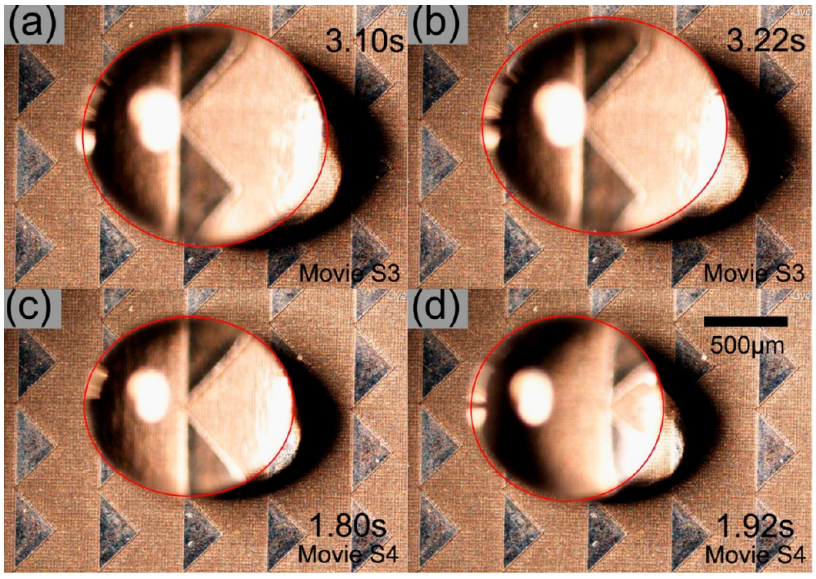

Figure 5. Evaporation behaviors of a water droplet on the t-surface at η = 0.25.

where f_1, θ_1 and f_2, θ_2 are the area fraction and CA for the superhydrophobic domain (spikes induced by a fs laser) and the hydrophobic domain (triangle, circle, and rhombus), respectively.

The typical TPCLs of water droplets on the t-/c-/r-surface are depicted in Figure 6, based on which the superhydrophobic

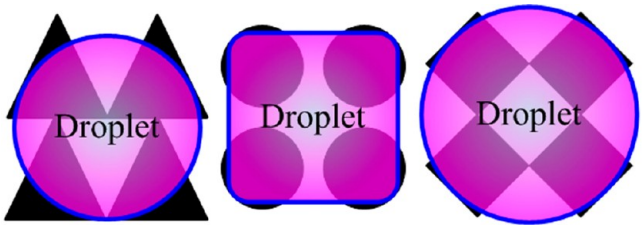

Figure 6. Typical triple-phase contact line of water droplet on the t-/c-/r-surface.

area fractions at different η are calculated and listed in Table 2, where also shows the experimental CAs and CAs calculated by eq 3. The CAs predicted by the Cassie–Baxter model are in good agreement with experimental CAs. It is also shown that a decrease in η actually leads to an increase in superhydrophobic domain area, thus rendering less water-adhesive force to a water droplet so that both CAs and V_L increase, as demonstrated in Table 1.

Sliding Angles. The sliding behavior of a droplet is an important factor in characterizing superhydrophobic surfaces.[40] As a sample is gradually tilted from the horizontal state, a droplet will become increasingly inclined downward. At a critical slope angle, the droplet will experience a sliding motion immediately along the inclined surface: this angle is defined as the sliding angle (SA).

As mentioned above, the 9-μL water droplet has the minimum water volume that enables a droplet to land on the t-/c-/r-surface at different η. So this volume droplet is selected to measure SAs on the t-/c-/r-surface. The dynamic behaviors of the moving droplets are recorded using a digital camera. Sequential photographs of the sliding water droplets are taken every 10 ms. The SAs are measured by tilting the samples at a rate of 1°/s until the droplet rolls off.

Figure 7a shows the measured SAs (colored dots) on the t-/c-/r-surface, as a function of hydrophobic area fraction (f_2, defined as $f_2 = 1 - f_1$, according to eq 3). It is evidently seen that SAs strongly depend on f_2 with little dependence on the hydrophobic domain pattern (triangle/circle/rhombus). As f_2 increases, SA increases from 5° (f_2 = 0.0517) to 37° (f_2 = 0.4209) on the r-surface. However, at f_2 = 0.7172, the droplet cannot slide away but remains attached to the surface, even when the sample is turned upside down. The SAs of the t-/c-surfaces show similar wetting trends to that of the r-surface. Therefore, the dynamic wetting properties herein, combined with the static wettabilities mentioned above, lead us to

Table 2. Area Fraction (f_1) of Superhydrophobic Domain on the t-/c-/r-Surface at Different η and Corresponding CAs[a]

	Triangle			Circle			Rhombus		
η	f_1	CA* (°)	CA (°)	f_1	CA* (°)	CA (°)	f_1	CA* (°)	CA (°)
0.5	0.3755	126	134	0.3559	125	136	0.2828	122	138
0.25	0.5745	136	146	0.5785	136	149	0.5791	136	144
0.1918	0.7520	147	150	0.6505	140	150	0.6643	141	149
0.1443	0.7895	149	151	0.7124	144	151	0.7409	146	152
0.1036	0.8571	155	155	0.8348	153	152	0.8549	155	153
0.067	0.9050	160	158	0.8850	158	155	0.9042	160	157
0.0329	0.9528	165	160	0.9394	164	160	0.9483	165	161

[a]CA* = contact angle calculated by the Cassie–Baxter (CB) model; CA = experimental contact angle.

dx.doi.org/10.1021/am3012388 | ACS Appl. Mater. Interfaces 2012, 4, 4905–4912

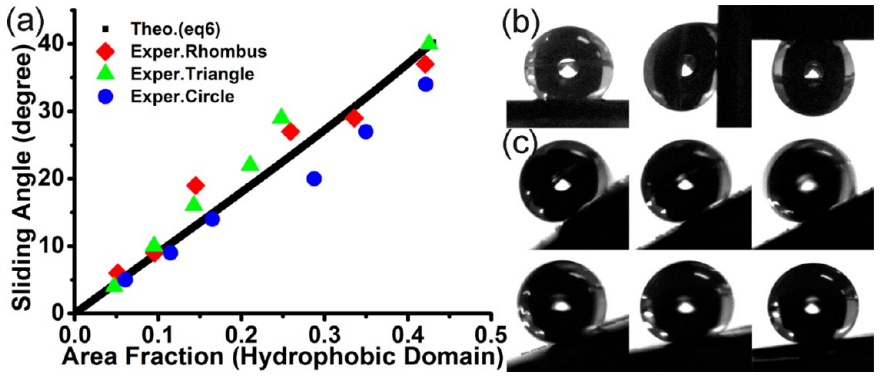

Figure 7. (a) Sliding angles as a function of hydrophobic area fraction (f_2). The color dots are the experimentally measured values, and the black line is the set of values predicted by the sliding angle model. (b) Optical images of the 9-μL water droplet on the r-surface at f_2 = 0.7172. (c) Morphologies of the sliding droplets with f_2 ranging from 0.0517 to 0.4209.

conclude that tunable adhesive surfaces can be realized by introducing regular patterns on a silicon surface at different hydrophobic area fractions.

To predict the sliding angle α of a droplet on a smooth surface, some equations have been established. Furmidge proposed a equation to calculate SA quantitatively:[41]

$$\rho g V \sin\alpha = 2Rk \tag{4}$$

where ρ and V respectively denote the droplet mass density and volume, g is the gravity acceleration, R is the radius of the wetted area, and k is a constant. Later, Frenkel[42] associated k with the advancing (φ_a) and receding angles (φ_r) and defined k as $\gamma_{LV}(\cos\varphi_r - \cos\varphi_a)$, where γ_{LV} denotes the interfacial tension between liquid and vapor. As a result, eq 4 becomes

$$\rho g V \sin\alpha = 2R\gamma_{LV}(\cos\varphi_r - \cos\varphi_a) \tag{5}$$

Recently, Lv et al.[43] proposed a new sliding angle model:

$$\sin\alpha = \frac{2\sqrt[3]{3}\,\gamma_{LV}\sqrt{2(1+\cos\phi_0) - (1+\cos\phi_0)^2 f}}{\rho g \sqrt[3]{\pi V^2}\sqrt[3]{4 - 3(1+\cos\phi_0)^2 f^2 + (1+\cos\phi_0)^3 f^3}} \quad (1+\cos\phi_0) f \tag{6}$$

where φ_0 is the intrinsic CA of smooth surface and f is the area fraction of substrate.

To investigate the relationship between SAs and the hydrophobic area fraction (f_2), the sliding angle model (eq 6) is employed. The simulated SAs are depicted in Figure 8a (presented later in this work), as denoted by the black line. It is shown that the SAs calculated by the sliding angle model are in good agreement with our experimental SAs, indicating that the sliding angle model may provide potentially theoretical fundation to design intelligent surfaces with different adhesive forces.

Sliding Mechanism Analysis. On the s-surface, a droplet is found to slide in a continuous manner (Figure 3). However, on the t-/c-/r-surface, it is found that water droplets slide in a discontinuous manner, similar to the droplet behaviors reported by Lv et al.[43] Taking the sliding behaviors of the 9-μL water droplet on the r-surface at f_2 = 0.4209 and 0.2591 as an example, the droplet morphologies at different times are shown in Figure 8, along with the TPCL evolution. As Figure 8a shows, when the slope angle of the surface equals SA, the droplet starts to move by conquering the FEBs where the

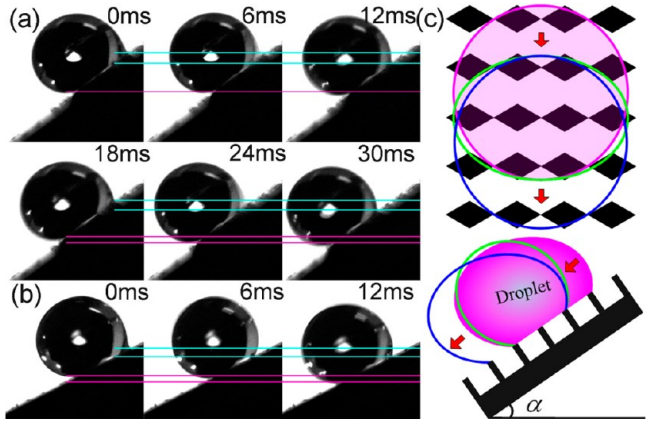

Figure 8. (a,b) Record of sliding process of a 9-μL water droplet on the r-surface at f_2 = 0.4209 and 0.2591. (c) Top view and side view of TPCL evolution on the r-surface at f_2 = 0.4209.

droplet anchors. First, the rear droplet detaches from the surface then quickly jumps to the former pattern and gets stick at its edge (0−12 ms). In this process, the front droplet remains adhering, as indicated by the purple line in Figure 8a. Subsequently, the front droplet advances with the rear adhering (12−18 ms). Later on, the rear droplet jumps and then gets pinning (18−30 ms), indicating that successive sliding motion will follow the same continuous sequence of the detachment-attachment process shown in the period of 0−18 ms. The sliding behaviors of a 9-μL droplet at f_2 = 0.2591, which shows very similar wetting trend as that which occurs at f_2 = 0.2591 on the r-surface (Figure 8b). The rear contact line experiences the depinning−repinning behavior at t = 6 ms and front contact line detaches at t = 12 ms. Either the detachment of a droplet in the rear part or in the front part is accompanied by the droplet attachment in the other direction.

The droplet sliding motion on the r-surface is associated with the variation of TPCL. The TPCL evolutionary process at f_2 = 0.4209 seen from top view and side view is depicted in Figure 8c. The rhombic array, seen from the side view, can be assumed to be the periodic pillars. Three different colored lines denote the TPCL at different times t. The pink line denotes the TPCL where a 9-μL droplet initially sits, the green line denotes the TPCL after the rear jump, and the blue line denotes the TPCL after the front jump. First, the rear contact line of the droplet jumps one rhombic row from up to down. And then the front contact line advances in one row with the rear contact line

dx.doi.org/10.1021/am3012388 | ACS Appl. Mater. Interfaces 2012, 4, 4905−4912

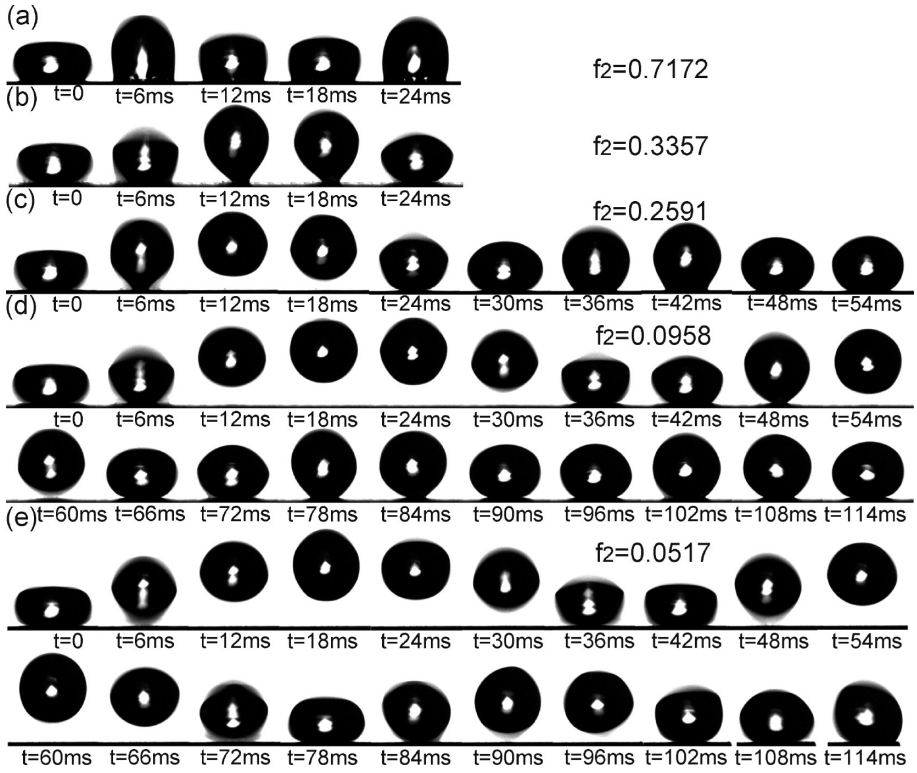

Figure 9. Time evolution of impact dynamics on the r-surface at f_2 = 0.7172, 0.3357, 0.2591, 0.0958, and 0.0517.

sticking to the surface. The droplet sliding behaviors on t-/c-surface follow the same dynamic wetting trend as the r-surface.

Water Droplet Rebound Behavior. Besides the static contact angle (CA) and sliding angle (SA), water droplet rebound behavior is another wetting property that can be used to characterize superhydrophobic surfaces,[44,45] which may have applications in self-cleaning, inkjet printing, and spraying techniques. It is expected that, by adjusting the area ratio of superhydrophobic domain to hydrophobic domain, tunable rebound behaviors can also be realized.

Snapshots in Figure 9 show the rebound behaviors of 10-μL water droplets on the r-surface at f_2 = 0.7172, 0.3357, 0.2591, 0.0958, and 0.0517. The 10-μL droplets are all released from a height of 3.5 mm above the surfaces. It is shown that surface roughness can greatly influence droplet impact on the r-surface and drop rebound behaviors can be tuned. When f_2 decreases from 0.7172 to 0.3357, the droplet sticks to the surface. However, as f_2 decreases, the droplet is more apt to rebound, which can be deduced from the highest point that the droplet reaches. Besides, the remaining part of the droplet left on the surface is more evidence to prove this droplet rebound trend. With the decrease of f_2, the droplet jumps higher, leaving less part on the surface. Further decreases in f_2 will give rise to the droplet rebound. At f_2 = 0.2591, the droplet begins to rebound but can only rebound once (Figure 9c). When f_2 reaches values of 0.0958 (Figure 9d) and 0.0517 (Figure 9e), the droplet rebounds twice and three times. The results indicate that, by varying the area ratio of superhydrophobic domain to hydrophobic domain, the rebound behavior can be apparently tuned, from triple rebound at small f_2 to a partial rebound at large f_2 with liquid sticking to the surface.

4. CONCLUSIONS

In conclusion, a method to realize tunable adhesive superhydrophobic surfaces by adjusting the surface morphology is demonstrated. By varying the area ratio of the superhydrophobic domain ($AR_{s\text{-}h}$) (spikes induced by a femtosecond laser) and hydrophobic domains (triangle, circle, and rhombus), both the static and dynamic wettabilities can be tuned. With gradually increasing $AR_{s\text{-}h}$, a water droplet is harder to land on the surface and is more apt to rebound, along with the decrease in sliding angle. Through the analysis of triple-phase contact lines, the wetting properties are found to be dependent on $AR_{s\text{-}h}$, but independent of pattern of hydrophoic domain. The Cassie−Baxter model and the sliding angle model are utilized to predict contact angles (CAs) and sliding angles (SAs). And the simulated results are in good agreement with the experimental data. This study not only presents a route for the fabrication of tunable adhesive superhydrophobic surfaces but also provides insights into the nature, function, and design of the sticky-to-slippery surfaces. The tunable adhesive surfaces can be potentially applied in cell adhesion modulation and water droplets' mobility control.

■ ASSOCIATED CONTENT

Supporting Information

Movies S1−S4. This material is available free of charge via the Internet at http://pubs.acs.org.

■ AUTHOR INFORMATION

Corresponding Author

*E-mail address: chenfeng@mail.xjtu.edu.cn.

Notes

The authors declare no competing financial interest.

■ ACKNOWLEDGMENTS

This work is surport by the National Science Foundation of China (under Grant No. 61176113), National High Technology R&D Program of China (under Grant No. 2009AA04Z305), and the Fundamental Research Funds for the Central Universities.

■ REFERENCES

(1) Li, X. M.; Reinhoudt, D.; Crego-Calama, M. *Chem. Soc. Rev.* **2007**, *36*, 1350−1368.
(2) Barthlott, W.; Neinhuis, C. *Planta* **1997**, *202*, 1−8.
(3) Jin, M. H.; Feng, X. J.; Feng, L.; Sun, T. L.; Zhai, J.; Li, T. J.; Jiang, L. *Adv. Mater.* **2005**, *17*, 1977−1981.
(4) Brushan, B.; Her, E. K. *Langmuir* **2010**, *26*, 8207−8217.
(5) Ishii, D.; Yabu, H.; Shimomura, M. *Chem. Mater.* **2009**, *21*, 1799−1801.
(6) Zhu, S. J.; Li, Y. F.; Zhang, J. H.; Lü, C. L.; Dai, X.; Jia, F.; Gao, H. N.; Yang, B. *J. Colloid Interface Sci.* **2010**, *344*, 541−546.
(7) Li, J.; Liu, X. H.; Ye, Y. P.; Zhou, H. D.; Chen, J. M. *J. Phys. Chem. C* **2011**, *115*, 4726−4729.
(8) Liu, X. J.; Cai, M. R.; Liang, Y. M.; Zhou, F.; Liu, W. M. *Soft Matter* **2011**, *7*, 3331−3336.
(9) Su, R. G.; Liu, H. B.; Kong, T.; Song, Q.; Li, N.; Jin, G.; Cheng, G. S. *Langmuir* **2011**, *27*, 13220−13225.
(10) Khedir, K. R.; Kannarpady, G. K.; Ishihara, H.; Woo, J.; Ryerson, C.; Biris, A. S. *Langmuir* **2011**, *27*, 4661−4668.
(11) Li, J.; Guo, Z.; Liu, J. H.; Huang, X. J. *J. Phys. Chem. C* **2011**, *115*, 16934−16940.
(12) Teisala, H.; Tuominen, M.; Aromaa, M.; Stepien, M.; MäKelä, J. M.; Saarinen, J. J.; Toivakka, M.; Kuusipalo, J. *Langmuir* **2012**, *28*, 3138−3145.
(13) Balu, B.; Berry, A. D.; Hess, D. W.; Breedveld, V. *Lab Chip* **2009**, *9*, 3066−3075.
(14) Zhao, N.; Xie, Q. D.; Kuang, X.; Wang, S. Q.; Li, Y. F.; Lu, X. Y.; Tan, S. X.; Shen, J.; Zhang, X. L.; Zhang, Y. J.; Xu, J.; Han, C. C. *Adv. Funct. Mater.* **2007**, *17*, 2739−2745.
(15) Mundo, R. D.; Nardulli, M.; Milella, A.; Favia, P.; D'Agostino, R.; Gristina, R. *Langmuir* **2011**, *27*, 4914−4921.
(16) Liu, K. S.; Jiang, L. *ACS Nano* **2011**, *5*, 6786−6790.
(17) Sarrat, B.; Pecheyran, C.; Bourrigaud, S.; Billon, L. *Langmuir* **2011**, *27*, 3174−3179.
(18) Zorba, V.; Stratakis, E.; Barberoglou, M.; Spanakis, E.; Tzanetakis, P.; Anastasiadis, S. H.; Fotakis, C. *Adv. Mater.* **2008**, *20*, 4049−4054.
(19) De Marco, C.; Eaton, S. M.; Levi, M.; Cerullo, G.; Turri, S.; Osellame, R. *Langmuir* **2012**, *27*, 8391−8395.
(20) Wu, B.; Zhou, M.; Li, J.; Ye, X.; Li, G.; Cai, L. *Appl. Surf. Sci.* **2009**, *256*, 61−66.
(21) Baldacchini, T.; Carey, J. E.; Zhou, M.; Mazur, E. *Langmuir* **2006**, *22*, 4917−4919.
(22) Zhang, D. S.; Chen, F.; Fang, G. P.; Yang, Q.; Xie, D. G.; Qiao, G. J.; Li, W.; Si, J. H.; Hou, X. *J. Micromech. Microeng.* **2010**, *20*, 075029.
(23) Chen, F.; Zhang, D. S.; Yang, Q.; Wang, X. H.; Dai, B. J.; Li, X. M.; Hao, X. Q.; Ding, Y. C.; Si, J. H.; Hou, X. *Langmuir* **2011**, *27*, 359−365.
(24) Zhang, D. S.; Chen, F.; Yang, Q.; Si, J. H.; Hou, X. *Soft Matter* **2011**, *7*, 8337−8342.
(25) Kietzig, A. M.; Hatzikiriakos, S. G.; Englezos, P. *Langmuir* **2009**, *25*, 4821−4827.
(26) Bandoki, P. B.; Benayoun, S.; Valette, S.; Beaugiradu, B.; Audouard, E. *Appl. Surf. Sci.* **2011**, *257*, 5213−5218.
(27) Her, T. H.; Finlay, R. J.; Wu, C.; Deliwala, S.; Mazur, E. *Appl. Phys. Lett.* **1998**, *73*, 1673−1675.
(28) Shen, M. Y.; Crouch, C. H.; Carey, J. E.; Mazur, E. *Appl. Phys. Lett.* **2004**, *85*, 5694−5696.
(29) Zhang, J.; Gao, X. F.; Jiang, L. *Langmuir* **2007**, *23*, 3230−3235.
(30) Shastry, A.; Case, M. J.; Bohringer, K. F. *Langmuir* **2006**, *22*, 6161−6167.
(31) Nosonovsky, M.; Bhushan, B. *Nano Lett.* **2007**, *7*, 2633−2637.
(32) Zander, N. E.; Orlicki, J. A.; Karikari, A. S.; Long, T. E.; Rawlett, A. M. *Chem. Mater.* **2007**, *19*, 6145−6149.
(33) Dorrer, C.; Rühe, J. *Langmuir* **2007**, *23*, 3179−3183.
(34) Forsberg, P. S. H.; Priest, C.; Brinkmann, M.; Sedev, R.; Ralston, J. *Langmuir* **2010**, *26*, 860−865.
(35) Priest, C.; Albrecht, T. W. J.; Sedev, R.; Ralston, J. *Langmuir* **2009**, *25*, 5655−5660.
(36) Zhang, X. Y.; Mi, Y. L. *Langmuir* **2009**, *25*, 3212−3218.
(37) Wong, T. S.; Ho, C. M. *Langmuir* **2009**, *25*, 12851−12854.
(38) Wenzel, R. N. *Ind. Eng. Chem.* **1936**, *28*, 988−994.
(39) Cassie, A. B. D.; Baxter, S. *Trans. Faraday Soc.* **1944**, *40*, 546−551.
(40) Krasovitski, B.; Marmur, A. *Langmuir* **2005**, *21*, 3881−3885.
(41) Furmidge, C. G. L. *J. Colloid Sci.* **1962**, *17*, 309.
(42) Frenkel, Y. I. J. *Exp. Theoret. Phys. (USSR)* **1948**, *18*, 659.
(43) Lv, C. J.; Yang, C. W.; Hao, P. F.; He, F.; Zheng, Q. S. *Langmuir* **2010**, *26*, 8704−8708.
(44) Jung, Y. C.; Bhushan, B. *Langmuir* **2008**, *24*, 6262−6269.
(45) Jung, Y. C.; Bhushan, B. *Langmuir* **2009**, *25*, 9208−9218.

■ NOTE ADDED AFTER ASAP PUBLICATION

This paper was published on the Web on August 28, 2012, with minor errors in ref 19. The corrected version was reposted on September 14, 2012.